1 Molybdenum Geochemistry in Salt Marsh Pond Sediments

2

3 Hutchings A. M[1]*., Basu A.[2], Dickson A. J.[2] and Turchyn A. V.[1]

4

5 ***Corresponding author (alechutchings24@gmail.com, +447825069166)**

6 **[1]Department of Earth Sciences, University of Cambridge, Downing Street, Cambridge, CB2**

7 **3EQ, UK**

8 **[2]Department of Earth Sciences, Royal Holloway, University of London, Egham, UK**

9

10 Abstract

11

12 The concentration and isotopic composition of sedimentary molybdenum (Mo) has been used

13 to distinguish different redox environments in modern marine settings and in the geological

14 record. In East Anglian salt marsh pond sediments, we report Mo concentrations and δ^{98}Mo

15 of porewater and sediments in three anoxic environments: (1) 'iron-rich' sediments

16 containing high concentrations of dissolved ferrous iron (up to 2 mM), (2) in 'sulfide-rich'

17 sediments containing very high concentrations of aqueous sulfide (up to 10 mM), and (3) in

18 sediments that we consider to be intermediate between 'iron-rich' and 'sulfide-rich'

19 conditions. In iron-rich sediments, we suggest iron speciation and iron mineralogy controls

20 the concentration and isotopic composition of Mo. Despite similar aqueous sulfide profiles,

21 the intermediate and sulfide-rich pond sediment have different porewater Mo concentrations

22 and δ^{98}Mo. In the intermediate pond sediment, we conclude that active breakdown of iron

23 oxides redistributes porewater Mo, observable as a peak of dissolved Mo (>100ppb), which

24 diffuses within the sedimentary porewaters. In the more evolved, sulfide-rich pond sediment,

25 we suggest that the concentration and isotopic composition of Mo is instead controlled by

26 solubility equilibrium with an Fe-Mo-S mineral species (e.g. $FeMoS_4$) due to similarities in

27 sediment and porewater δ^{98}Mo throughout the sediment column. The sedimentary δ^{98}Mo is

28 higher in sulfide-rich and intermediate pond sediment (mean = 1.66‰, range = 0.98–1.92‰)

29 than in iron-rich pond sediment (mean = 1.10‰, range = 0.28–1.65‰) with both ponds

30 having sedimentary δ^{98}Mo that is lower than seawater. The maximum sedimentary δ^{98}Mo

31 observed in these anoxic sediments, which is 0.5-0.7‰ lower than seawater, appears to be set

32 by Fe-Mo-S equilibration with ambient thiomolybdate species. We suggest diagenetic

33 overprinting can cause more efficient capture of pond water Mo and causes sediment δ^{98}Mo

34   of originally iron-rich pond sediment to evolve to higher values when sulfide is added to the

35   porewater.

36

1. Introduction

38

39   The concentration and isotopic composition of molybdenum (Mo), a redox sensitive trace

40   metal, has been used to understand paleoredox conditions in Earth history (Arnold, 2004;

41   Reinhard et al., 2013; Dickson, 2017) and to trace modern biogeochemical redox reactions

42   (Skierszkan et al., 2017; Skierszkan et al., 2019). In the modern ocean, Mo predominantly

43   exists as the soluble molybdate ion (MoO_4^{2-}), which behaves conservatively with a residence

44   time of 440 kyr (Miller et al., 2011). In most oceanic sediments, this molybdate ion is

45   removed inefficiently by adsorption onto iron (Fe) and manganese (Mn) oxides in

46   oxic/suboxic conditions. In the presence of aqueous sulfide, however, removal of dissolved

47   Mo is far more efficient due to the progressive thiolation of MoO_4^{2-} species to more insoluble

48    $MoO_{(4-x)}$ (Erickson and Helz, 2000). Consequently, enrichments of sedimentary Mo in the

49   rock record have been used to suggest water columns that are locally euxinic, containing free

50   aqueous sulfide (Scott and Lyons, 2012).

51

52   The isotopic composition of sedimentary Mo adds further insight into redox environments.

53   The molybdenum isotope ratio is reported in delta notation relative to NIST-SRM-3134 +

54   0.25‰ (Equation 1) (Nägler et al., 2013).

55

56   (1) $\delta^{98}Mo = \left[\left(\frac{(^{98}Mo/_{95}Mo)_{Sample}}{(^{98}Mo/_{95}Mo)_{NIST-SRM-3134}} \right) - 1 \right] * 1000 + 0.25 \ [‰]$

57

58   No known chemical reaction preferentially removes heavier Mo isotopes to the sedimentary

59   phase, thus the δ^{98}Mo of sedimentary Mo is lower than the water from which it derives, while

60   the residual porewaters have been observed to have a higher δ^{98}Mo (McManus et al., 2002;

61   Kendall et al., 2017). As a consequence, seawater δ^{98}Mo (δ^{98}Mo = 2.3‰) is higher than any

62   surface sediment signature (Siebert et al., 2003; Nägler et al., 2011; Nakagawa et al., 2012).

63   The process of Mo removal into sediments differs based on the geochemistry of the water

64   column, sediment, and the porewater, and each process imparts a characteristic δ^{98}Mo into

65   the sediment. These differences in sedimentary δ^{98}Mo allow us to distinguish between

66   sediments deposited under different redox conditions.

67

68   In sedimentary environments where a sulfide fraction (comprising H_2S, HS^- and S^{2-}) is

69   absent in both the overlying water column and in the porewater, molybdate adsorbs to Fe and

70   Mn oxides present at the sediment-water interface. Molybdenum isotope fractionation occurs

71   when a tetrahedral coordination of MoO_4^2 in solution changes to a distorted octahedral Mo-

72   containing surface complex during adsorption (Wasylenki et al., 2011). Different Mo isotope

73   fractionation factors (Δ^{98}Mo) are associated with different Fe and Mn oxide minerals, the

74   largest isotope fractionation being associated with adsorption onto Mn oxides (Δ^{98}Mo =

75   δ^{98}Mo$_{Seawater}$ - δ^{98}Mo$_{MnOxide}$ = 2.2–3.3‰) (Barling and Anbar, 2004; Wasylenki et al., 2011).

76   Molybdenum isotopic fractionation during adsorption depends on the Fe mineral in question,

77   with Mo isotopic fractionation factors ranging from Δ^{98}Mo = 0.83‰ for magnetite (Fe_3O_4)

78   up to Δ^{98}Mo = 2.19‰ for hematite (Goldberg et al., 2009). Variations in the mineralogy of

79   the iron minerals have been posited as a potential driver of the range of δ^{98}Mo measured in

80   bulk oxic sediments (Goldberg et al., 2012). While oxic environments cover most of the

81   modern ocean floor (>80%), the slow rate of adsorption, combined with the propensity of Fe

82   and Mn oxides to be reduced during sediment burial under reductive conditions and release

83   any adsorbed Mo, means that they play a disproportionately smaller role in removing Mo

84   from the modern ocean than their area would suggest (Shaw et al., 1990; Scott and Lyons,

85   2012; Reinhard et al., 2013).

86

87   In the presence of aqueous sulfide, the molybdate ion (MoO_4^{2-}) is progressively thiolated to

88   oxythiomolybdate species $Mo(O_xS_{4-x})^{2-}$ and terminally to tetrathiomolybdate (MoS_4^{2-}) at a

89   rate of reaction on the order of hours, days, weeks and months for each sequential reaction in

90   Equation 2 respectively. At and above 11 μM H_2S (aq), tetrathiomolybdate becomes the

91   dominant aqueous Mo species (Erickson and Helz, 2000).

92

93   (2) $MoO_4^{2-} \rightarrow MoO_3S^{2-} \rightarrow MoO_2S_2^{2-} \rightarrow MoOS_3^{2-} \rightarrow MoS_4^{2-}$
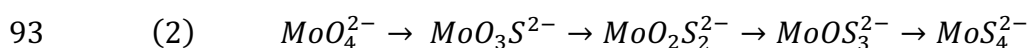
94

95   While thiomolybdate species are more efficiently scavenged onto particles than molybdate

96   species, the pathway of sequestration of the various thiomolybdate species (Equation 2)

97   remains debated. Pyrite has been discounted as a major host for Mo in sediments where

98   pyrite is present, though Mo could potentially adsorb to other sulfide minerals (Chappaz et

al., 2014). Organic carbon and Mo have a strong empirical association (Algeo and Lyons, 2006; McManus et al., 2006), which has led some authors to suggest that thiomolybdate is scavenged into the sediment by organic matter (Lyons et al., 2009; Dahl et al., 2017). Other authors have suggested this link may not be causal, and have instead advocated that the formation of an iron-sulfur-molybdenum complex—which ultimately becomes sequestered as an $FeMoS_4$ species—is the main output of Mo in euxinic sediments (Helz et al., 2011; Vorlicek et al., 2018; Helz and Vorlicek, 2019). Regardless of the mechanism, the presence of aqueous sulfide in porewaters causes dissolved Mo to be near-quantitatively removed to sediments, hence bulk sediment δ^{98}Mo in sulfidic sediments tends to be higher than non-sulfidic sediments. Whilst it was initially thought that dissolved Mo was quantitatively captured in euxinic environments, it has since been found that there is a limiting aqueous Mo concentration present dependent on pH, sulfide concentration and availability of free iron (Helz et al., 2011). As such, the δ^{98}Mo in sediment where aqueous sulfide is present in porewater can be up to 0.5‰ lower than the dissolved δ^{98}Mo (Nägler et al., 2011).

We still lack a fundamental understanding of the specific reaction pathways driving sediment δ^{98}Mo in both Fe/Mn dominated environments and in aqueous sulfide dominated environments. Factors such as periodic water column redox changes, particle reactivity in the water column and organic matter likely all play a role in the δ^{98}Mo of the sediment that is ultimately buried (Dahl et al., 2010; Helz et al., 2011; Scholz et al., 2013; Scholz et al., 2017; King et al., 2018; Scholz et al., 2018). In order to fully utilise the potential of the Mo isotope and concentration proxy, we must first understand the behaviour of Mo in well constrained redox environments.

The sediments beneath saline ponds in East Anglian salt marshes, England (**Fig. S1**) may offer insight into the mechanisms behind Mo sequestration and its isotopic composition under varying redox conditions. In East Anglian salt marshes, we have observed two types of pond sediment characterised by different redox conditions. In some pond sediments, rates of bacterial iron reduction are high, resulting in high concentrations (up to 2 mM) of ferrous iron. In other pond sediments, as close as 5 m apart, microbial sulfate reduction is the dominant microbial reaction, resulting in high concentrations (up to 10 mM) of aqueous sulfide (Hutchings et al., 2019). The redox conditions in these two types of pond sediment have been previously reported (Pye et al., 1990; Mills et al., 2016; Hutchings et al., 2019; Antler et al., 2019; Wilkening et al., 2019; Lin et al., 2019; van de Velde et al., 2020). Hence,

133   by measuring both porewater and sediment Mo and the associated δ^{98}Mo, we can probe the

134   relationship between the redox cycles of iron and sulfur and the chemical reactions involving

135   Mo. For this study, we have collected sediment cores from one pond identified as iron-rich, a

136   second pond identified as sulfide-rich and a third pond suspected to be an intermediate

137   between iron and sulfide pond chemistry. By using high resolution sediment and porewater

138   measurements of Mo concentration and isotopic compositions, we are able to understand both

139   active geochemical processes (captured by the porewater) and time integrated geochemical

140   processes (captured by the sediment). Our objective is to determine how the behaviour of Mo

141   is controlled by iron and sulfur cycles in marine and marginal marine sediments. Our

142   hypothesis is that Mo concentrations and isotopic composition will reveal the chemical and

143   mineralogical reactions occurring in salt marsh pond sediment that are not evident in iron or

144   sulfur measurements.

145

146   **2. Methods**

147

148   **2.1. Field site**

149

150   Cores for this work were collected from the sediment beneath saline ponds in Abbotts Hall

151   Farm salt marsh, Essex, UK (**Fig. S1**). Our current hypothesis is that all ponds begin with

152   iron-rich chemistry due to a high iron mineral content, sourced from the nearby Cretaceous

153   iron-rich cliffs, and that some pond sediments progress to sulfide-rich pond sediment with

154   time. Upon addition of a sufficient amount of organic carbon, sulfate reduction can become

155   the dominant reaction if all available Fe(III) sources are reduced (Hutchings et al., 2019). If

156   enough sulfide is generated from sulfate reduction, either in one large event or in enough

157   individual events, then a switch in sediment geochemistry can occur and the porewater begins

158   to accumulate large amounts of dissolved sulfide in place of ferrous iron (see Appendix 1 for

159   full details). It has been suggested that non-linear effects related to the burrowing of

160   macrofauna may cause feedbacks which will determine which state a pond sediment will end

161   as (van de Velde et al., 2020).

162

163   **2.2. Field methods**

164

165 Pond sediment classified as iron-rich (sampled Nov. 2018), pond sediment classified as

166 sulfide-rich (sampled May 2018) and pond sediment classified as intermediate (sampled May

167 2018) were sampled using 30 cm PVC push cores (**Fig. S1**). To acquire enough porewater for

168 Mo isotope measurements, two cores were pushed into the pond sediment simultaneously

169 within one metre of each other. Hutchings et al. (2019) previously showed that pond

170 sediment geochemistry does not vary over these distances, especially if both cores are a

171 similar distance from the pond edge. A wider core (ID = 102 mm) was used for all sediment

172 analysis, porewater major cation, porewater trace metal analysis and Mo isotope

173 measurements and a narrower core (ID = 65 mm) was used for porewater sulfur, iron, and

174 anion analysis. Once cores were placed, each could be lifted in turn without disturbing the

175 sediment or water within the other core.

176

177 Sediment was extracted using 2 mL cut-syringes. Roughly 15 mL of porewater was extracted

178 for each sample from the core at 2 cm resolution using Rhizons attached to a 5 mL syringe.

179 Based on porosity measurements (Table 1), this sampling resolution corresponds to an

180 extraction of 17−35% of the total porewater volume at each depth increment. To prevent over

181 extraction at the top of the core, where porosity is greatest, syringes from all depths were

182 allowed to fill to 5 mL before more sample was pulled at any depth increment. Sediments

183 were sampled prior to porewater extraction to prevent porewater mixing. All sediments were

184 digested immediately after extraction to prevent any further reaction with remaining

185 porewater.

186

Sediment type	Depth (cm)	Porosity
Sulfur	7	0.873
Sulfur	31	0.718
Intermediate	10	0.859
Intermediate	34	0.637
Iron	4.5	0.828
Iron	18.5	0.732
Iron	28.5	0.573

187

188 **Table 1 –** *Porosity measurements for random samples in each of the three cores. >3g of wet*

189 *sediment was weighed, dried completely in a convection oven, and reweighed. Porosity was*

190 *calculated using 1.035 g cm^{-3} for saline water density and 1.90 g cm^{-3} and 2.00 g cm^{-3} for*

191 *sulfide- and iron-rich dry sediment density respectively (measured in (van de Velde et al.,*
192 *2020)).*

193

194 Pond water overlying the pond sediment was collected from the three ponds during the
195 November 2018 sampling. The pond water was sampled at a later period due to the extreme
196 drying that occurred in the ponds during May 2018 sampling which resulting in a <2 cm
197 water column. We assume that, given the regular tidal flushing of these ponds (at least
198 monthly), only minor $\delta^{98}Mo$ distillation will occur under typical conditions. The effect of the
199 near-complete evaporation of the pond water on our porefluid results in May 2018 is
200 unknown. Acid cleaned 125 mL LDPE bottles were submerged and sealed under the pond
201 water to ensure no air bubbles. Pond water was filtered within 24 hours and acidified with 1
202 mL of concentrated HNO_3.

203

204 **2.3. Analytical measurements for geochemical characterisation of the system**

205

206 The porewater pH was measured using a Mettler Toledo with a Five Easy plus pH probe.
207 Fe(II) was determined spectrophotometrically (Thermo Aquamate UV-Vis) according to the
208 method of (Stookey, 1970) with an uncertainty of 0.4%. Immediately after extraction, an
209 amount of porewater was added to 100 µL of ferrozine to produce a colour within the
210 calibrated adsorption range. In sulfide-rich cores, aqueous sulfide in remaining porewater in
211 the smaller core was fixed in 250 µL (20 wt%) zinc acetate immediately and an aliquot was
212 taking after rigorous shaking (to ensure the precipitate was equally distributed) to measure
213 sulfide concentrations. Sulfide concentrations were determined spectrophotometrically using
214 the (Cline, 1969) method with relative uncertainty of ~2% and a detection limit of 1 µM. The
215 remaining solution was separated into the aqueous phase (containing sulfate) and the sulfide-
216 containing ZnS phase. For the aqueous phase, major anions (Cl^-, SO_4^{2-}, NO_3^-) were measured
217 by ion chromatography (Thermo Scientific Dionex ICS5000+) with an uncertainty of 2%
218 based on standard repeats. All porewaters analysed for cations were stored in HCl/HNO_3
219 cleaned plastic ware. Major cations were measured on an ICP-OES (Agilent) with 3% error
220 based on replicate of standards. Porewaters were matrix matched to Na concentration before
221 analysis of trace metals on an ICP-MS (Element) using artificially matched standards.
222 Standard addition was used on multiple samples to check for differing matrix effects.

223

224 **2.4. Sediment characterisation**

225

Weighed ~500 mg aliquots of wet sediment were digested in 4 mL of concentrated aqua regia
for >24 hours at 115°C. Samples were centrifuged and the eluent was carefully pipetted for
analysis. For three samples in the iron-rich core, adsorbed Mo fraction was leached from ~1g
of wet sediment using 20 mL of 0.1M phosphate solution. This mixture was shaken for at
least 24 hours, centrifuged, and the eluent was extracted. The remaining sediment was rinsed
with a (<1 mM) NaCl solution, centrifuged, and the eluent was discarded. The sediment was
left to dry overnight and weighed before being digested as per the method above. The
phosphate concentration used in this leaching step is well in excess of experiments where
>99% of Mo (as molybdate and thiomolybdate) was desorbed from goethite and >85% was
desorbed from pyrite as phosphate ions compete with molybdate/thiomolybdate for surface
sites on the mineral (Xu et al., 2006). Total sedimentary iron and manganese was determined
by ICP-MS with internal standards. A constant quantity of indium (In) was added to each
sample to adjust for matrix effects of acid digests.

A sediment core was taken from the iron-rich and sulfide-rich pond in May 2019 to
determine sediment mineralogy. We assume that the changes to the mineralogy of sediment
are minimal over the course of a year, given the salt marsh sediment accreted over the last
millennium, though we cannot exclude minor variation in authigenic mineralogy over this
sampling hiatus. Sediments were taken from a number of depths and immediately transferred
to an anaerobic glove box. A thin layer of sediment was smeared on glass slides and left to
dry under anaerobic conditions. Samples were measured by X-Ray Diffraction (XRD) within
30 minutes of being removed from the glovebox. XRD was conducted on a Philips PW1830
X-Ray diffractometer from 0-90 degrees. Mineral peaks were identified using Match!
software and mineral abundances were calculated using Rietveld analysis.

2.5. Mo isotope and concentration determination

Precisely weighed digested sample aliquots were spiked with ^{100}Mo-^{97}Mo double spike for a
spike/sample ratio of ~0.3 and evaporated to dryness. For sediment digests, 0.2 mL of 4 M
HCl was added to replace molybdenum nitrate salts with molybdenum chloride salts and the
solution was evaporated to dryness. Porewaters required redissolution in 3 mL of 4 M HCl
for the same step due to the high salt content. Mo was purified from the digested sample
matrix using the single anion exchange technique of Pearce et al. (2009) as modified by

259   Dickson et al. (2016) to separate Zn. The δ^{98}Mo was determined by MC-ICP-MS (Thermo

260   Neptune Plus). Spiked NIST-3134 standards were run every three samples and a digested

261   Open University solution Mo standard was run every ten samples. The long-term external

262   reproducibility of the method is ±0.06 per mil (2 S.D.) based on replicate digestions of the

263   SDO-1 standard over the course of ~18 months. For all runs, seawater was within analytical

264   uncertainty of the accepted seawater value (2.34 ± 0.10‰) (Nägler et al., 2013) and

265   procedural blanks were less than 1 ng. Reported molybdenum concentrations were calculated

266   by isotope dilution with the ^{100}Mo-^{97}Mo double spike.

267

268   **3. Results**

269   **3.1. Iron and sulfur redox chemistry**

270   Visible mineralogical changes (as seen in the colour of the sediment) in the iron-rich core

271   coincide with differences in porewater and sedimentary concentrations of Fe and Mn (**Fig. 1,**

272   **2**). We divide the iron-rich core into four zones separated by these coloured boundaries (**Fig.**

273   **2, Table 2**). Dissolved sulfide is below detection limit in the iron-rich core and SO_4/Cl is

274   marginally higher than in local seawater (**Fig 1a,b**). Dissolved ferrous iron is relatively

275   constant in Zones I and II (~1 mM), increases in Zone III to ~1.8 mM, before decreasing to

276   ~0.2 mM from 20–30 cm (Zone IV) (**Fig. 1c**). Sedimentary Fe concentrations are highest at

277   the surface and generally increase with decreasing porewater Fe(II) with depth (**Fig. 1d**). Iron

278   mineralogy is a combination of ferrihydrite, pyrite, mackinawite, goethite, and—in Zone 4

279   only— hematite (**Fig 3a, Table 3**). Dissolved Mn is considerably higher than in the other

280   cores and increases from 0.02 mM to 0.14 mM by 27 cm depth (**Fig. 1e**). Sedimentary Mn is

281   roughly 1000 times lower than sedimentary Fe (**Fig. 1f**) and is characterised as birnessite

282   ($H_{2.72}Mn_{0.5}Na_{0.364}O_{2.544}$) (**Table 3**).

283
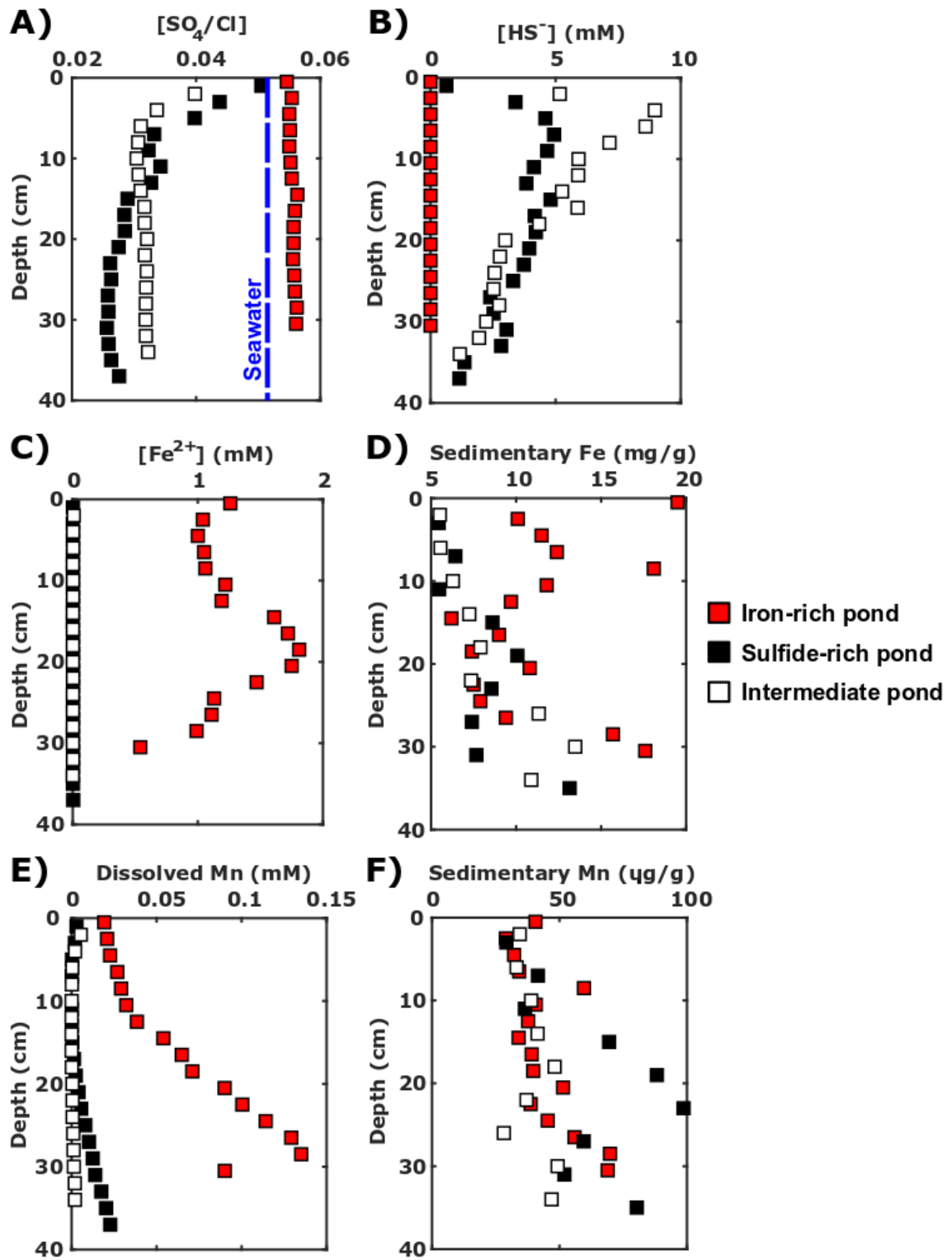
Figure 1 – *Geochemical data for the iron-rich, sulfide-rich and intermediate cores: a)*

Dissolved SO$_4$/Cl ratios. Blue dashed line indicates typical seawater values. b) Dissolved

sulfide concentrations. c) Dissolved Fe²⁺ concentrations d) Sedimentary Fe content. e)

Dissolved Mn in porewaters. f) Sedimentary Mn content. The analytical error bars for these

analyses are smaller than the data symbols used.
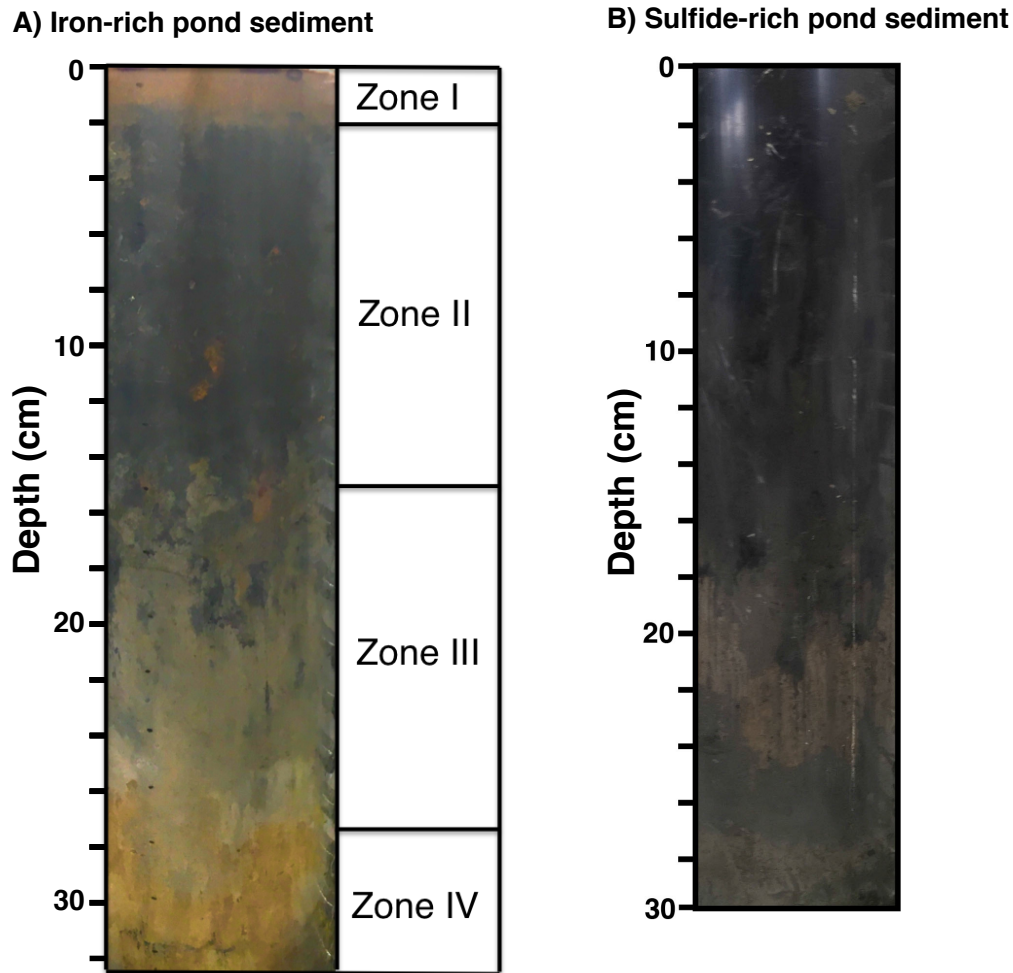
Figure 2 *– a) Photo of the iron-rich pond sediment core before extraction of porewaters and sediment. Picture shows the coloured zones present in the iron-rich pond sediment (see Table 2 for characteristics of zones). b) Photo of the sulfide-rich pond sediment core before extraction of porewaters and sediments. The intermediate pond sediment was near-identical in appearance to the sulfide-rich pond sediment. Brightness has been increased in both photos to make the zones appear more clearly.*

Sediment zone	Depth	Colour	Features
Zone I	0–2 cm	Orange-red	Variable colours based on different pond sediment[1]. Authigenic phases of iron are abundant.
Zone II	2–15 cm	Black	Worm burrows present in patches (bioirrigation)[2]. Orange sediment line the burrows. Burrows are more abundant at 12 cm than at 4 cm (**Fig. S2 and S3**).
Zone III	15–25 cm	Pale grey	A mixed boundary occurs between Zone II and Zone III. Some burrows penetrate into the upper portion of this zone, fully terminating at 21 cm depth.
Zone IV	25–<31 cm	Grey/orange mottled	Crunchy texture with orange speckled appearance. Gravel was present in the sediment just below this core.

302 **Table 2 –** *Characteristics for the four defined zones of the iron-rich pond sediment core. [1]See*

303 *Hutchings et al. (2019) for a classification scheme which uses, in part, surface sediment*

304 *colour. [2]See Appendix 3 for evidence (**Fig. S2; Fig. S3**)*

A) Iron-rich pond sediment
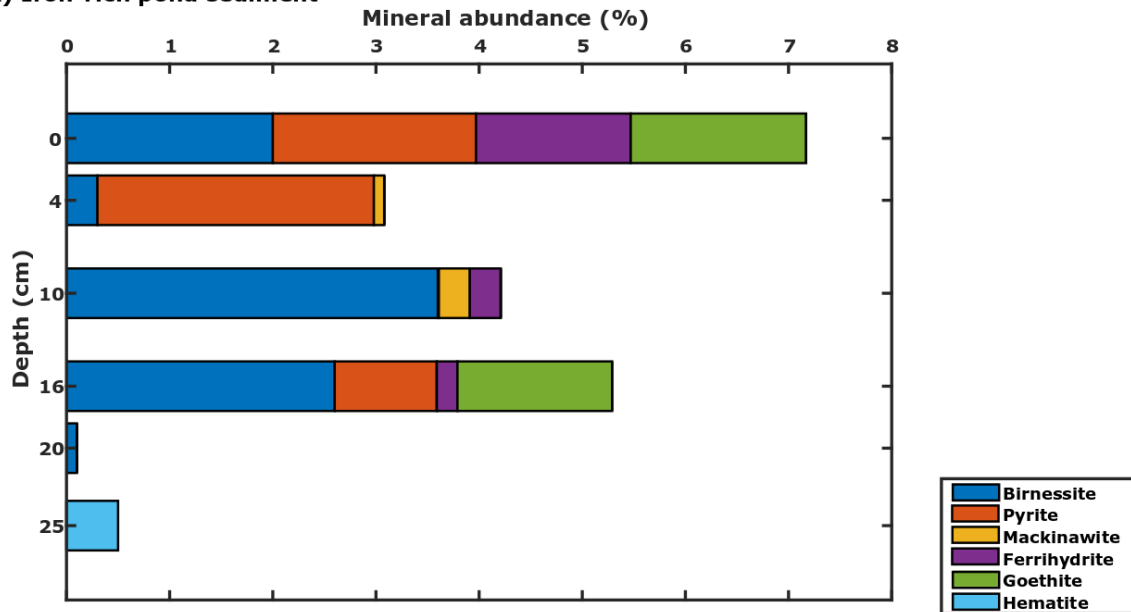
B) Sulfide-rich pond sediment

305
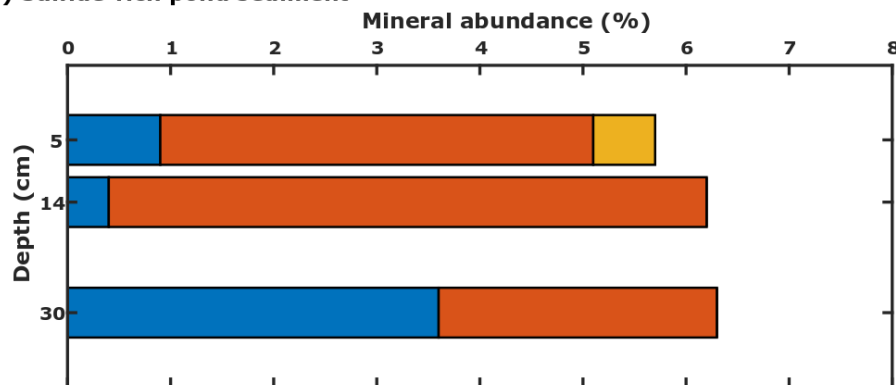
Figure 3 – Rietveld analysis of XRD mineralogical data for pond sediments analysed at various depths in the (a) iron-rich pond sediment and (b) sulfide-rich pond sediment. Only Fe and Mn oxides are shown here (full mineralogical assemblage is given in Table 3). Abundances are corrected for the removal of evaporitic salt minerals ($MgSO_4$ and KCl) which represent the porewater fraction. For individual spectra of each depth sample, see supplementary information (**Fig S4-S12**)

312

313

314

315

316

317

318

319

320

Depth (cm)	DoC	Quartz	Halite	Illite	MgSO$_4$	Pyrite	Birnessite	Mackinawite	Ferrihydrite	Goethite	KCl	Hematite
Sulfide-rich pond												
5	26.72	45	32.4	16.1	2.7	2.7	0.6	0.4	0	0	0	0
14	26.53	51.3	22.6	21.3	0	4.5	0.3	0	0.01	0	0	0
30	29.62	54.4	5.9	33.8	0	2.5	3.4	0	0	0	0	0
Iron-rich pond												
0	21.57	37.1	28.6	28.9	0	1.4	1.4	0	1.1	1.2	0.2	0
4	29.32	38.4	29	30.3	0	1.9	0.2	0.1	0	0	0	0
10	26.51	43.8	22.7	30.3	0	0.01	2.8	0.2	0.2	0	0	0
16	33.77	48	18.5	29	0	0.8	2.1	0	0.2	1.2	0.3	0
20	40.16	63.7	10.5	25.7	0	0	0.1	0	0.01	0	0	0
25	39.9	78.8	0.1	20.7	0	0	0	0	0	0	0	0.5

321

322 **Table 3 -** Summary of identified minerals from XRD analysis. Estimated proportions for each depth point are conducted using Rietveld analysis

323 for a best fit to the data and are given in percentage proportion. Abbreviations (DoC = Degree of crystallinity). For individual spectra of depth

324 profiles, see Fig. S4-S12.

325

326

327   Instead of the coloured zoning in the iron-rich core, the sediment in the sulfide-rich and

328   intermediate cores fades from black at the surface to dark grey at depth (**Fig. 2b**). The sulfide

329   and intermediate cores have comparable porewater sulfide concentrations with a peak at 5–10

330   cm between 5 and 9 mM and a decrease below this to ~1 mM at 35 cm (**Fig. 1b**). Maximum

331   porewater sulfide concentration is higher in the intermediate pond-sediment than in the

332   sulfide-rich pond sediment (9 mM and 5 mM respectively). The SO_4/Cl ratio decreases from

333   seawater until a constant ratio is reached in both the sulfide-rich core and intermediate core

334   (**Fig. 1a**). The constant SO_4/Cl is lower and deeper for the sulfide-rich pond (0.026)

335   compared to the intermediate pond (0.032). Only trace amounts of ferrous iron were detected

336   in both cores and dissolved manganese concentrations are much lower than in the iron-rich

337   core (**Fig. 1c, e**). Sedimentary Fe is roughly similar between the sulfide-rich and intermediate

338   core; there is a consistent increase with depth from 5 mg/g to roughly 12 mg/g (**Fig. 1d**).

339   Almost all of the sedimentary iron present in the sulfide-rich pond sediment is present as a

340   combination or pyrite and mackinawite (**Fig. 3b, Table 3**). Similar to the iron-rich pond

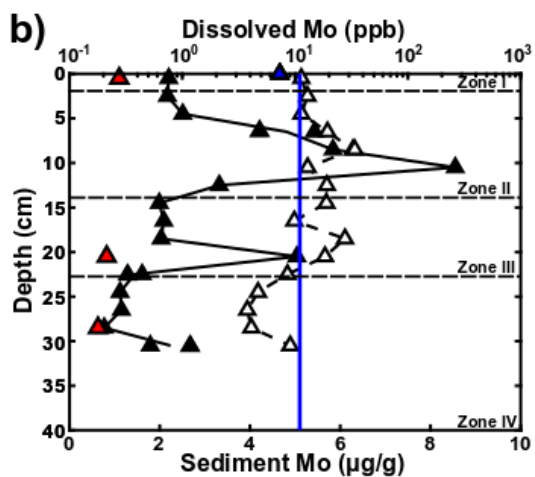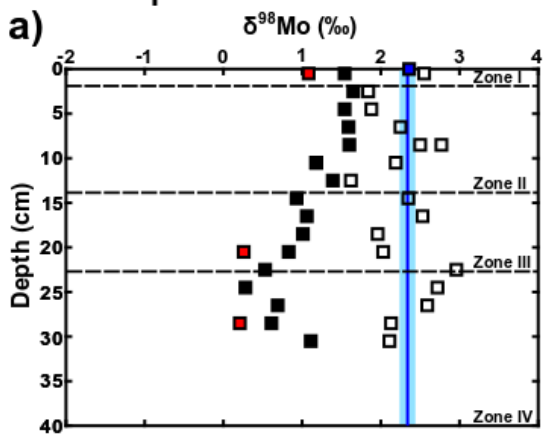341   sediment, birnessite ($H_{2.72}Mn_{0.5}Na_{0.364}O_{2.544}$) is the main Mn hosting mineral.

342

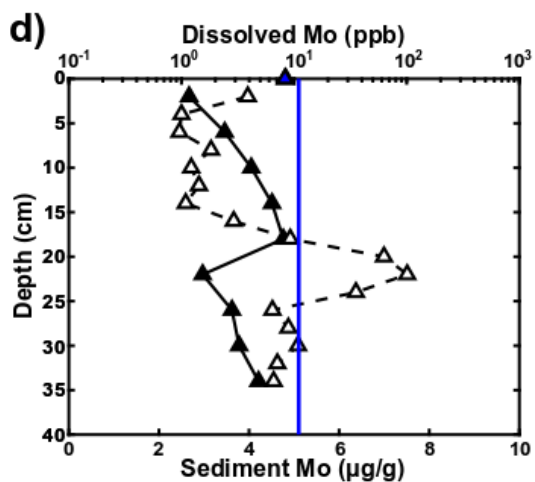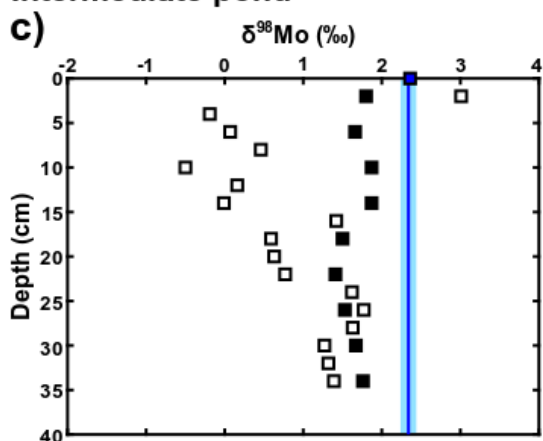343   **3.2. Molybdenum concentration and isotopes**

344

345   **3.2.1. Iron rich core**

346   Both porewater and sedimentary Mo concentrations decrease with depth in the iron-rich core

347   (**Fig. 4b**). A large increase in sedimentary Mo content at 5–12 cm and at 18–23 cm are are

348   observed with a noticeable increase in porewater Mo at the same depths. Phosphate-leached

349   sediment—theoretically removing any Mo adsorbed to the sediment (Xu et al., 2006)—has a

350   lower Mo content which decreases with depth from 1.1 μg/g at 0.5 cm to 0.6 μg/g at 28.5 cm.

351   Porewater $\delta^{98}Mo$ is higher than sediment $\delta^{98}Mo$ at all depths (**Fig. 4a**). Pond water $\delta^{98}Mo$ is

352   within analytical uncertainty of seawater $\delta^{98}Mo$ and at all depths, porewater Mo fluctuates

353   around this seawater value. Below 18 cm, porewater $\delta^{98}Mo$ anticorrelates with sedimentary

354   $\delta^{98}Mo$. Sedimentary $\delta^{98}Mo$ decreases from 1.65‰ (2.5 cm) to 0.28‰ (24.5 cm) and increases

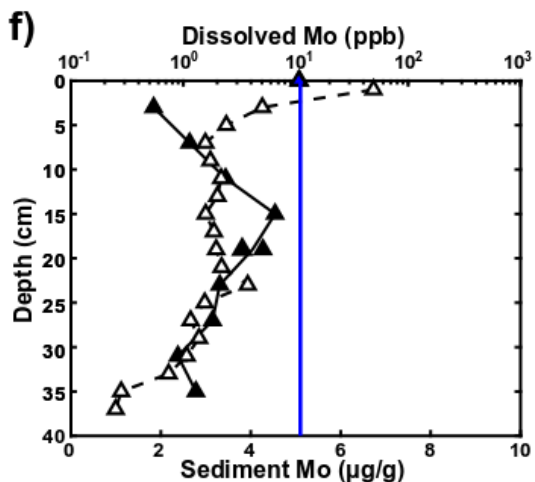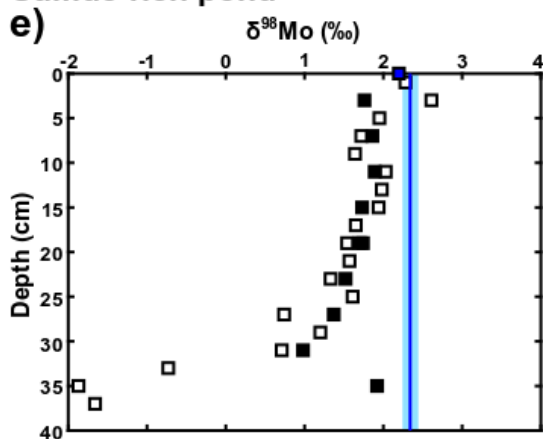355   again below this depth to 1.11‰ (30.5 cm) (**Fig. 4a**).

Iron-rich pond

a) δ⁹⁸Mo (‰) versus Depth (cm), with Zone I, Zone II, Zone III, Zone IV markers

b) Dissolved Mo (ppb) / Sediment Mo (µg/g) versus Depth (cm), with Zone I, Zone II, Zone III, Zone IV markers

Intermediate pond

c) δ⁹⁸Mo (‰) versus Depth (cm)

d) Dissolved Mo (ppb) / Sediment Mo (µg/g) versus Depth (cm)

Sulfide-rich pond

e) δ⁹⁸Mo (‰) versus Depth (cm)

f) Dissolved Mo (ppb) / Sediment Mo (µg/g) versus Depth (cm)

Legend

δ⁹⁸Mo	Concentration
☐ Porewater	△ Porewater
■ Sediment	▲ Sediment
■ Pond water (blue)	▲ Pond water (blue)
■ Leached sediment (red)	▲ Leached sediment (red)

356
357

358

359 **Figure 4 –** *For all plots, the solid blue line indicates typical seawater values and the shaded*

360 *light blue line refers to the uncertainty on the seawater value (±0.10‰)* (Nägler et al., *2013*).

361 *Uncertainty on $\delta^{98}Mo$ is ±0.06‰ which is within the area of the sample squares. Sediment*

362 *and porewater $\delta^{98}Mo$ from the (a) iron-rich pond, (c) intermediate pond and, (e) sulfide-rich*

363 *pond. Leached sediments were sediment samples treated with 0.1M phosphate solution (red*

364 *symbols). Sediment Mo content (bottom axis) and porewater Mo concentration (top axis) in*

365 *the (b) iron-rich pond t, (d) intermediate, and (f) sulfide-rich pond.*

366

367 **3.2.2. Sulfide-rich and intermediate core**

368

369 Porewater Mo concentration and $\delta^{98}Mo$ differs between the sulfide-rich core and the

370 intermediate core despite both having high concentrations (up to 10 mM) of aqueous sulfide.

371 In the sulfide-rich core, porewater Mo concentrations decrease from 40 ppb at the surface to

372 <1 ppb at 35 cm (**Fig 4f**). Concurrently, porewater $\delta^{98}Mo$ also decreases from 2.2‰ to -

373 2.0‰, a large range encapsulating the range of $\delta^{98}Mo$ in nearly all known environmental

374 samples (**Fig 4e**).

375

376 In the intermediate core, porewater Mo concentration drops below 3 ppb and mean $\delta^{98}Mo$ is

377 0.00±0.50‰ between 4 and 14 cm (**Fig 4c,d**). From 15–25 cm, there is a large increase in

378 porewater Mo concentration to ~101 ppb (over 8x that of seawater). This increase is

379 associated with a shift in porewater $\delta^{98}Mo$ to 0.5–1.5‰. Below this depth, porewater Mo

380 concentration decreases to ~8 ppb with a $\delta^{98}Mo$ of 1.4‰. We observe a similar sedimentary

381 enrichment (4 μg/g) of Mo at 15–20 cm in both the sulfidic and intermediate cores. Sediment

382 $\delta^{98}Mo$ ranges from 0.98–1.92‰ (mean = 1.64‰) and 1.41–1.87‰ (mean = 1.67‰) in the

383 sulfide-rich core and intermediate core, respectively (**Fig 4c,e**).

384

385 **4. Discussion**

386

387 In this discussion, we first consider the chemical reactions and Mo isotope fractionation in

388 the iron-rich pond sediment. We then compare the geochemistry of the two ponds, termed

389 'sulfide-rich' and 'intermediate', that contain comparable levels of porewater sulfide. If pond

390 sediment chemistry is changing from iron-rich to sulfide-rich as previously hypothesized,

391   there is a chance that the two different sulfide-containing pond sediments may capture

392   different stages in this transition. Finally, we compare sediment δ^{98}Mo in the iron-rich pond

393   sediment with the sulfide-rich pond sediment to understand the role of diagenesis on the

394   sediment δ^{98}Mo.

395

4.1. Molybdenum behaviour in the iron-rich pond sediment

396

397

398   Four different redox zones are found in the iron-rich pond sediment and their colour is

399   controlled by the mineralogy of iron in the sediment which, in turn, relates to the overall

400   redox state in each of the zones (**Fig. 1, Fig. 2**). Differences in porewater and sediment Mo

401   and their corresponding δ^{98}Mo track these redox zones closely (**Fig 4 a,b**). At all sampled

402   depths, porewater δ^{98}Mo is higher than sediment δ^{98}Mo.

403

404   Since dissolved sulfide concentrations are less than 1 μM, the dominant aqueous Mo species

405   present in these iron-rich sedimentary porewaters will be MoO_4^{2-} (Erickson and Helz, 2000).

406   High dissolved Fe^{2+} concentrations prevent the accumulation of aqueous sulfide in these

407   sediments as any sulfide generated through transient microbial sulfate reduction will be

408   rapidly titrated by the excess dissolved iron to form iron sulfide species (Canfield et al.,

409   1992). We surmise that iron oxides are likely to be the species which scavenge the majority

410   of MoO_4^{2-}, despite the presence of Mn-oxides, because the sedimentary content of Fe is 500

411   times higher than Mn (**Fig. 1**) and sedimentary δ^{98}Mo increases with decreased dissolved Mn

412   concentrations ($r^2 = 0.81$)—the opposite direction to what we would expect if Mn oxides

413   were influencing δ^{98}Mo (**Fig. S13**) (Wasylenki et al., 2011).

414

415   At the sediment surface (0-2 cm depth), the reaction of ferrous iron with oxygen produces a

416   reddish, iron oxide rich layer comprising minerals such as ferrihydrite and goethite (Zone I)

417   (**Fig. 2, Fig. 3a**). The MoO_4^{2-} ion from seawater, in the overlying pond water, will be

418   adsorbed as a polymolybdate complex onto these minerals at the sediment-water interface

419   (Wasylenki et al., 2011). Adsorption to Fe oxides is supported by the fact that the phosphate-

420   stripped sediments (removing the adsorbed fraction from sediments) contain significantly

421   (~50%) less Mo than the same sample which was only digested in aqua regia. Furthermore,

422   the Δ^{98}Mo$_{pw-sed}$ = 1.0‰ in Zone I is similar to the Mo isotope fractionation factor during

423   adsorption of Mo to ferrihydrite (1.11±0.15 ‰, Goldberg et al., 2009) and is similar to the

424   offset recorded by surface ferruginous sediments underlying Peruvian seawater (between 0.82

425   to 1.04‰ lower than seawater δ^{98}Mo) (Scholz et al., 2017). Regular flushing of pond water

426   with seawater prevents any increase in δ^{98}Mo of the pond water by isotopic distillation, so the

427   pond water retains a δ^{98}Mo signature similar to that of seawater. We therefore expect the

428   surface sediment δ^{98}Mo to have a consistent offset from pond water δ^{98}Mo.

429

430   Mineralogical analysis (XRD) suggests that the sediment in Zone II, beneath Zone I, contains

431   significant concentrations of pyrite and mackinawite (**Fig. 3a**), staining the sediment black.

432   The sediment in this zone is bioirrigated by worms (e.g. *Polychaete* spp.) which introduce

433   oxygen-rich seawater from the overlying pond to this zone. An active iron redox cycle is set

434   up when oxic water reoxidizes ferrous iron back into Fe(III) minerals, evidence of which can

435   be seen in the rust around bioirrigation burrows (**Fig. S2, S3**) (Antler et al., 2019). This rapid

436   redox recycling of iron gives the geochemical impression that iron reduction is limited since

437   porewater Fe^{2+} is lower in Zone II (**Fig. 1c**). It is likely that MoO_4^{2-} tracks this iron cycle as it

438   is constantly desorbed and reabsorbed onto Fe^{3+} minerals which are being reduced and then

439   reoxidised respectively (**Fig. 5**). This zone has a constant sediment δ^{98}Mo (~1.4‰), similar to

440   the surface sediment, therefore the molybdate ion adsorbed in the sediment phase is

441   effectively 'well mixed'. This observation implies that the residence time of the molybdate

442   ion in the Zone II porewater is much shorter than the sedimentation rate, or other changes to

443   the sedimentary redox zonation.
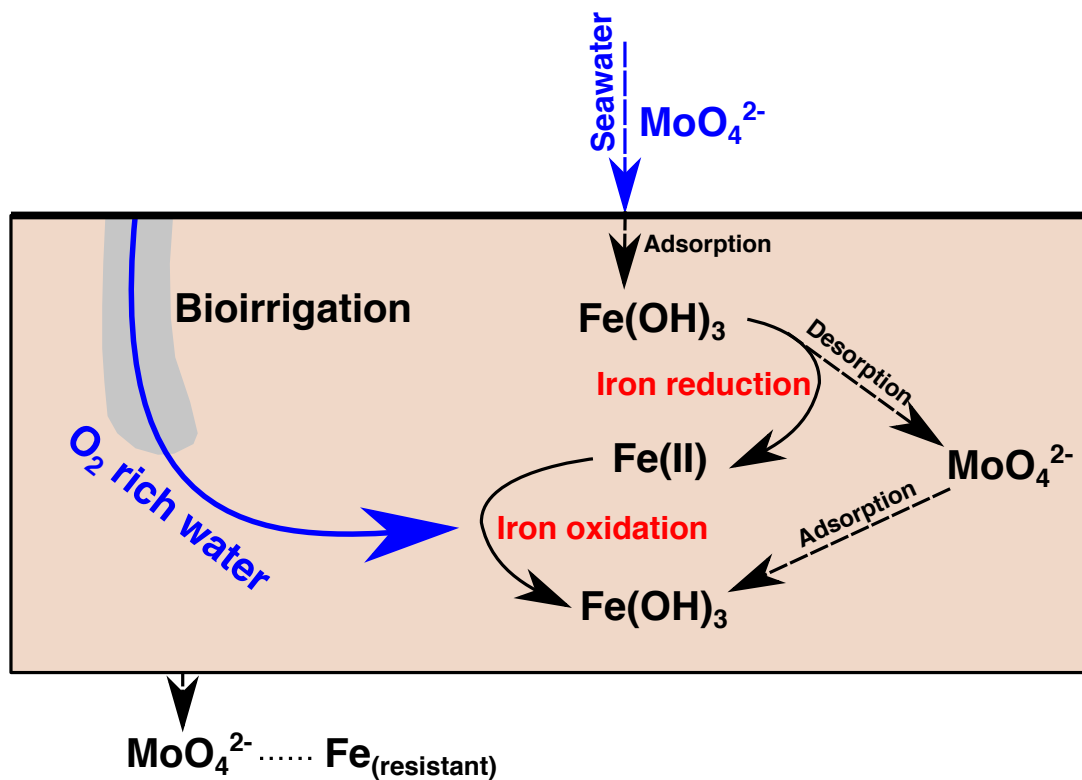
Figure 5 – *Schematic of processes affecting Mo behaviour in Zone II of the iron-rich pond sediment. Molybdate is directly adsorbed from seawater onto iron and manganese oxides. When sedimentary Mo reaches Zone II, the molybdate ion will be desorbed and resorbed onto the Fe^{3+} minerals (e.g. $Fe(OH)_3$) as they are dissolved and re-precipitated respectively. This active iron cycling is set up due to bioirrigation caused by worms in the sediment sub-surface. Only molybdate adsorbed to species which are not bioavailable for iron reduction will be buried below Zone II into Zone III, hence sedimentary Mo content becomes enriched in Zone II.*

The enrichment in sedimentary Mo content seen in Zone II (**Fig. 4b**) occurs as a result of this iron cycling. Below Zone II, the absence of bioirrigation means that there is no mechanism to reoxidise Fe^{2+} and therefore less Fe^{3+} minerals are present to adsorb any desorbed molybdate. As desorption of molybdate is greater than adsorption of molybdate in Zone III, there will be a net transfer of molybdate from the sediment phase to the dissolved phase. This dissolved porewater molybdate will diffuse upwards into Zone II, where the greater presence of Fe^{3+} minerals would re-adsorb it and thus concentrate sedimentary Mo. Sedimentary Mo enrichments have long been associated with euxinic conditions, although some combination of environmental conditions can cause an increased Mo content in the absence of aqueous sulfide (Scholz et al., 2017). The sediment concentrations here correspond to wet,

464 unconsolidated sediments as opposed to the dry rock powders reported in rocks assumed to

465 have been deposited under euxinic water. When corrected for porosity and compaction, the

466 high sedimentary Mo content enrichments we observe caused by iron cycling in salt marshes

467 would be comparable to euxinic settings in the rock record (Scott and Lyons, 2012) For this

468 sedimentary Mo enrichment to be preserved however, there would have to be some

469 mechanism (such as an increase in the sedimentation rate) which would prevent sedimentary

470 Mo from being affected by further iron cycling.

471

472 In Zone III, molybdate ions are desorbed from sediment into the porewater where the

473 dissolved Mo then diffuses away in porewaters. This process is most noticeable in the sharp

474 decline of sedimentary Mo concentrations between Zones II and III **(Fig. 4b)**. We suggest

475 that the δ^{98}Mo of the remaining sediment is lower in this zone as the more labile, or

476 microbially accessible, Fe^{3+} phases are first reduced, leaving behind Fe^{3+} phases which are

477 more crystalline and resistant to bacterial iron reduction. We note the change in the Fe

478 mineralogy with depth from XRD, from a ferrihydrite-goethite assemblage (less crystalline)

479 at ~15cm depth, to one dominated by haematite (more crystalline) by ~25 cm **(Fig. 3a)**. Less

480 crystalline iron minerals, such as ferrihydrite (Δ^{98}Mo$_{fluid-mineral}$ 1.1‰) typically have higher

481 δ^{98}Mo than more crystalline iron minerals (e.g. Δ^{98}Mo$_{fluid-minera}$ haematite = 2.2‰) (Goldberg

482 et al., 2009). The decline in sediment δ^{98}Mo from Zone II to Zone III is therefore readily

483 explained by a change in Fe mineralogy.

484

485 In Zone IV, the sediment δ^{98}Mo increases with depth whereas the porewater δ^{98}Mo decreases.

486 These changes could be due to the presence of less crystalline Fe minerals (Goldberg et al.,

487 2009), though this is not supported by XRD data **(Fig 3a, Table 3)**. Porewater δ^{98}Mo may

488 also be influenced by mixing with some groundwater flow below Zone IV. The presence of

489 subsurface flows beneath salt marsh sediment has been suspected but the nature of the fluid

490 remains enigmatic (Mills et al., 2016; Hutchings et al., 2019; Antler et al., 2019).

491

492 **4.2. Molybdenum behaviour in sulfide-rich pond sediment and intermediate pond**

493 **sediment**

494

495 **4.2.1. Sulfide-rich pond and intermediate pond porewater**

496

497   Lower porewater Mo concentrations in sulfide-rich ponds are explained by the rapid

498   thiolation of molybdate species with aqueous sulfide and the subsequent scavenging of these

499   thiomolybdated species (Equation 2). Other than a near-surface difference, the deeper

500   porewater aqueous sulfide concentrations are similar in both pond sediments, meaning sulfide

501   concentrations alone would not allow us to distinguish geochemical differences between

502   these two pond sediments (**Fig 1b**).

503

504   The chemical reactions sequestering Mo in sediment in contact with aqueous sulfide are

505   debated (Helz and Vorlicek, 2019). One posited phase which could host Mo in such

506   sediments is an Fe-Mo-S mineral with the empirical formula ($FeMoS_4$, *jordisite*), a phase

507   which has been identified using X-ray absorption spectroscopy (Vorlicek et al., 2018). To test

508   the likelihood of $FeMoS_4$ as a host phase, we use the model described in Helz et al. (2011) to

509   predict porewater Mo concentrations if pore fluid Mo is assumed to be in equilibrium with

510   FeS and an Fe-Mo-S phase. The model uses measured values of ionic strength, Ca and Mg

511   activity, total dissolved sulfide and the pH of the solution to predict the dissolved Mo

512   concentrations, as previously done in lakes (Helz et al., 2011). This model is valid for these

513   sedimentary environments if we assume that the rate of transport of Mo, thought to be mostly

514   diffusive, is slower than the thermodynamics needed for the formation of $FeMoS_4$.

515

516   The model predicts Mo concentrations similar to the measured values between 5 and 25 cm

517   in the sulfide-rich pond sediment (**Fig. 6a**). This coincides with a portion of the sediment core

518   where sediment $\delta^{98}Mo$ and porewater $\delta^{98}Mo$ are very similar (**Fig 4e**). If the model is

519   correctly predicting that porewater $\delta^{98}Mo$ in this part of the sediment core is being controlled

520   by solubility with an $FeMoS_4$ phase, then the similarity between the sediment and porewater

521    $\delta^{98}Mo$ can be explained in one of two ways. First, if there is an equilibrium isotope

522   fractionation factor associated with this chemical equilibrium, dissolved Mo in association

523   with the $FeMoS_4$ phase has a $\delta^{98}Mo$ value fortuitously similar to the sediment $\delta^{98}Mo$

524   generated at deposition. This could occur due to the temporal difference between the

525   porewater and the sedimentary pool, with the sedimentary pool reflecting a longer-term

526   recorder of the diagenetic history of the pond. An alternate explanation is that when dissolved

527   Mo is controlled by association with an $FeMoS_4$ mineral, any mechanism which operates

528   between the sediment and dissolved phase does so with negligible equilibrium isotopic

529   fractionation. For this to be true, equilibrium isotopic fractionation would have to be

530   sufficiently small or slow to prevent an isotopic offset being generated between porewater

531 and sediment. While we do not know the specifics of this mechanism, the data presented here

532 suggests that that in environments where porewater δ^{98}Mo follows sediment δ^{98}Mo closely

533 with depth, this may reflect a system where porewater Mo is in chemical and isotopic

534 equilibrium with the FeMoS$_4$ phase.

535

536
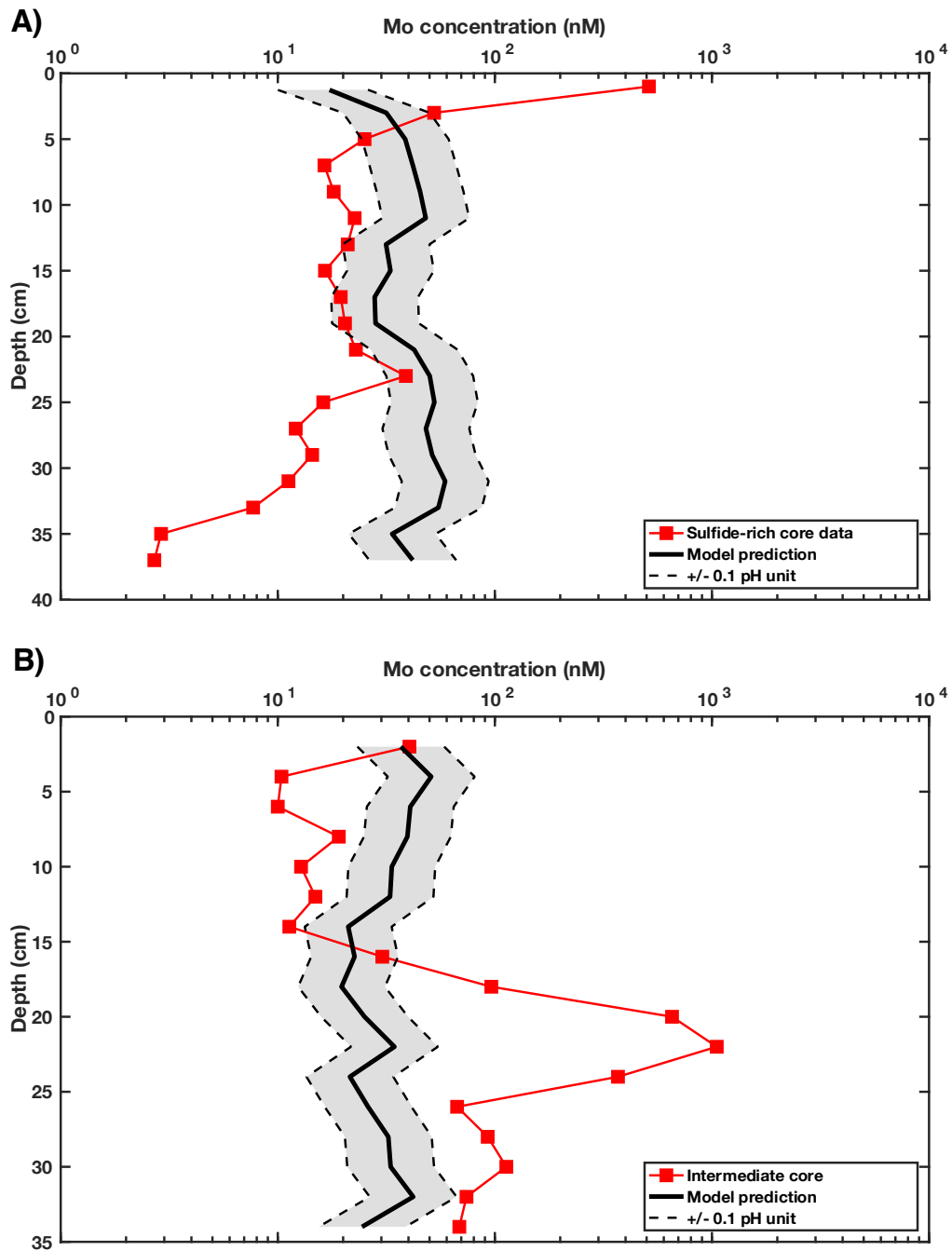
537

538 **Figure 6** – *a) Calculation of Mo concentration in porewaters using the model described in*

539 *Helz et al. (2011) for aqueous systems in equilibrium with an FeMoS$_4$ phase within (a) the*

545

546   Since pH in the model has a disproportionately large role in determining Mo concentration,

547   the model overestimates the amount of dissolved Mo present below 25 cm depth (Helz et al.,

548   2011) (**Fig. 6a**). The low concentrations (~0.5 ppb) of measured dissolved Mo below 25 cm

549   depth have the lowest $\delta^{98}Mo$ measured in this study and may reflect the fluctuations of the

550   depth of the redox boundary between iron reduction and sulfate reduction. Deeper sediments

551   recovered from sulfide-rich ponds contain a boundary where aqueous sulfide becomes

552   depleted and ferrous iron becomes present, presumably marking the end of the zone in which

553   sulfate reduction outcompetes iron reduction (**Fig. S14**). If this boundary depth changes

554   during seasonal variations in the intensity of microbial sulfate reduction, the sulfide and

555   ferrous iron concentration of porewater in this portion of the sedimentary column is likely to

556   vary. The rapidity of these changes could produce intermediate thiomolybdates (MoO_3S^{2-},

557   $MoO_2S_2^{2-}$ and $MoOS_3^{2-}$) with lower $\delta^{98}Mo$ which could become scavenged and released later.

558   This effect could temporarily produce porewater $\delta^{98}Mo$ lower than sediment $\delta^{98}Mo$. The

559   transient dissolution of such low concentrations of intermediate thiomolybdates would only

560   minimally affect the recorded sedimentary $\delta^{98}Mo$.

561

562   In the intermediate core at depths below 25 cm, similarity between porewater and sediment

563   $\delta^{98}Mo$ suggests that porewater could be associated with an Fe-Mo-S-containing phase,

564   similar to the sulfide-rich pond sediment (**Fig, 4c**), however the model underestimates the

565   dissolved Mo concentration (**Fig 6b**). This discrepancy may represent analytical errors on the

566   measured pH which, as mentioned above, has a large effect on the predicted dissolved Mo

567   (Helz et al., 2011). There may also be ligands—not considered in the model—which stabilise

568   thiomolybdate ions in the dissolved phase. At depths shallower than 25 cm however, the

569   model completely fails to accurately predict the dissolved Mo profile (**Fig. 6b**). In particular,

570   a peak in porewater Mo concentrations between 18–24 cm, over eight times seawater

571   concentration, cannot be explained by solubility equilibrium with an Fe-Mo-S phase. We

572   suggest that this peak of dissolved Mo reflects the release of adsorbed Mo during the sulfide-

573   induced reductive breakdown of residual iron and manganese oxides which were formed

574   when the pond sediment was initially iron rich. The depth at which dissolved Mo

575   concentrations are highest (23 cm) would therefore reflect the active dissolution zone. It

576   would be expected that this dissolution front progresses downwards through the sediment as

577   sulfide concentrations accumulate in the porewater from the surface sediment downwards

578   with time. Upon release, the desorbed molybdate ion will be rapidly converted to

579   thiomolybdate whilst concurrently diffusing away from the zone of peak dissolution.

580   Consistent with this interpretation, δ^{98}Mo of the porewater at the depth where Mo

581   concentrations are highest (0.63 ± 0.14‰) is similar to the sediment δ^{98}Mo signature

582   recorded at the same depth (0.83‰) in the iron-rich pond sediment.

583

584   Removal of thiomolybdates through particle reactivity appears most effective from 5 to 15

585   cm in the intermediate core—the depth that coincides with the highest aqueous sulfide

586   concentrations. As porewater Mo concentrations are below what is predicted for equilibrium

587   with an Fe-Mo-S phase, we can assume that either the thermodynamic model for Fe-Mo-S

588   breaks down at higher aqueous sulfide concentrations or some other species—possibly the

589   iron sulfide minerals present (**Fig 3b**) or organic matter—is helping to facilitate more

590   effective sequestration of thiomolybdate. Two possible mechanisms could cause the low

591   δ^{98}Mo in porewater located at this depth: (1) the dissolution of manganese oxides in the

592   presence of aqueous sulfide which would release isotopically low (-0.7‰) molybdate or, (2)

593   the formation of intermediary thiomolybdate species during a rapid change in sulfide

594   concentrations. Regardless of the mechanism, the lower δ^{98}Mo of the porewater than the

595   sediment suggests a temporal decoupling of the processes governing sediment and porewater

596   isotopic compositions.

597

598   We have found that concentrations and isotopic composition of porewater Mo reveal

599   differences between two sediment cores with similar aqueous porewater sulfide

600   concentrations (**Fig. 1b**). In the intermediate pond sediment, we suggest the model is not

601   applicable as active release of Mo from dissolved Fe and Mn oxides is ongoing. In sulfide-

602   rich pond sediments, where there is a deeper and more established zone of microbial sulfate

603   reduction, we suspect that aqueous sulfide has been concentrated for long enough so that

604   most Fe and Mn oxides have been broken down. In this type of sediment, Mo behaviour is

605   controlled by solubility equilibrium with the $FeMoS_4$ phase as described in Helz et al. (2011).

606   This difference would suggest that $FeMoS_4$ is the ultimate phase in which Mo is hosted

607   within the sulfide-rich pond sediments.

4.2.2. Sulfide-rich and intermediate pond sediment – diagenetic overprinting

Sedimentary enrichments of Mo content have been used to identify sulfidic environments in the geological record (Scott and Lyons, 2012). In this study, the total Mo content is not significantly different between iron-rich and sulfide-rich pond sediments (**Fig 4b,d,f**). This is because ponds are relatively short-lived systems with seawater Mo being the only input. Therefore, even if there is a rapid uptake of Mo from the overlying pond water, there is not enough time to significantly enrich Mo in the sulfide-rich sediments over their iron-rich counterparts. Whereas the iron-rich pond contains a very localised enrichment of sedimentary Mo from 5–15 cm due to active iron cycling (see above), sedimentary Mo is more constant with depth in the ponds containing aqueous sulfide in the porewater. This constancy is due to the redistribution of Mo as iron oxides are dissolved.

Sediment δ^{98}Mo recorded in restricted basins with a water column containing >11μM dissolved H_2S, such as the Black Sea, records the δ^{98}Mo of the input flux (Neubert et al., 2008; Nägler et al., 2011). In these environments, where the water column above the sediment is restricted, isotopic distillation of the Mo in the water column causes water-column δ^{98}Mo to increase above typical seawater values (>2.8‰ in the Black Sea) and thus sediment evolves by Rayleigh fractionation to approach seawater values. For isotopic distillation of the water column to occur, the sequestration rate of Mo must therefore be greater than the rate in which fresh Mo (with a seawater δ^{98}Mo value) is replenished in the above water column. The short residence time (days–months) of the water column in the Norfolk ponds means that the seawater δ^{98}Mo is not recorded in the sediment δ^{98}Mo and are consistent instead with certain continental margin sediments (Poulson et al., 2006; Poulson Brucker et al., 2009). The consistent replenishment of seawater to the pond prevents distillation of the pond water δ^{98}Mo signature (i.e. the replenishment rate is faster than the sequestration rate). The offset that is proposed to exist during sequestration of thiomolybdate species (~0.7‰) is therefore expressed, and the sediment δ^{98}Mo becomes lighter than the seawater δ^{98}Mo (Nägler et al., 2011). It is likely therefore, that the δ^{98}Mo of sediment in contact with aqueous sulfide lies on a continuum between 1.6‰ and 2.3‰, with lower δ^{98}Mo associated with more regular flushing of the overlying water.

641   The average sediment δ^{98}Mo is higher in the sulfide-rich (1.65‰) and intermediate core

642   (1.67‰) compared to the iron-rich core (1.10‰). Given that all ponds in the salt marsh are

643   hypothesized to have had initially iron-rich sediment chemistry, we suggest that the δ^{98}Mo of

644   the pond sediment reflects the degree of diagenetic overprinting caused by exposure to

645   sulfidic conditions over time. As described above, when aqueous sulfide becomes present in

646   porewaters, molybdate ions previously adsorbed to iron oxides are released as the iron

647   minerals breakdown (creating localised peaks in pore fluid Mo). The released molybdate is

648   converted to a thiomolybdate species and then re-scavenged back into the sedimentary phase,

649   causing the sediment δ^{98}Mo to evolve to higher values (**Fig. 7**). As the pond ages, the

650   presence of aqueous sulfide will continually capture Mo from pond water with a higher

651   δ^{98}Mo than when the pond sediment contained ferric iron minerals. The redistribution of

652   sedimentary Mo during the breakdown of these iron minerals will speed up the isotopic

653   overprinting process at depth in pond sediment. This process will continue until the original

654   lower pond sediment δ^{98}Mo present when the pond sediment was iron-rich is completely

655   overprinted (**Fig. 7**). At this point, we would expect a constant sediment δ^{98}Mo profile with

656   depth corresponding to the capture of thiomolybdate species (1.6–1.8‰). This mechanism

657   can explain the δ^{98}Mo measured in sediments in the sulfide-rich and intermediate cores.

658   Above 15 cm, a constant δ^{98}Mo reflects the capture of thiomolybdate species. Below 15–20

659   cm in both sediment cores, the sediment δ^{98}Mo is lower by roughly 0.3–1‰. This likely

660   reflects mixing between residual molybdate ions adsorbed to iron oxides and the newly added

661   tetrathiomolybdates and intermediate thiomolybdate species.

662
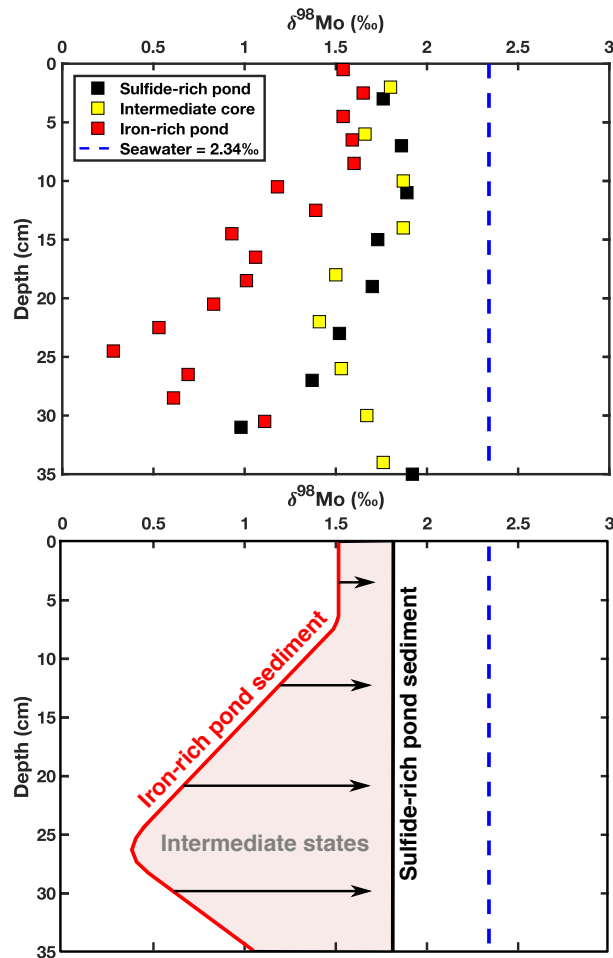
Figure 7 – *a) Comparison of $\delta^{98}Mo$ in sediments from the three ponds. Blue dashed line represents seawater values. b) Schematic describing the temporal evolution of sediment $\delta^{98}Mo$ in ponds in East Anglian salt marshes. Pond sediment begins as iron-rich (red solid line) until sulfate reduction becomes the dominant metabolism. At this point, the sediment $\delta^{98}Mo$ at all depths will become higher due to overprinting since sulfide-rich conditions sequester higher $\delta^{98}Mo$. Sediment $\delta^{98}Mo$ will therefore lie somewhere in the pink shaded zone (defined as intermediate states). Over time, overprinting of the sediment $\delta^{98}Mo$ will be complete, and a constant $\delta^{98}Mo$ will be expected around 1.7±0.1‰, a value typical of sediments with high aqueous sulfide in the porewater phase (Kendall et al., 2017).*

Our results suggest sedimentary $\delta^{98}Mo$ can be overprinted if the redox chemistry of the sedimentary system changes during early stage diagenesis. Original redox conditions which would be classified as 'ferruginous' are overprinted when porewaters become enriched in aqueous sulfide. The implication of this diagenetic change is that geochemical conditions

680 recorded at the time of deposition are not preserved if there is an authigenic redistribution of
681 the Mo and/or a change in the mechanism which captures dissolved Mo into sediment. East
682 Anglian salt marsh ponds appear very susceptible to this geochemical transition, likely due to
683 the close energy availability between sulfate reduction and iron reduction at circumneutral
684 pH (Bethke et al., 2011).
685

5. Conclusions

687
688 Salt marsh systems provide a well characterized redox environment to study Mo behaviour.
689 High resolution measurements of both porewater and sediment Mo allow us to isolate
690 individual mechanisms affecting Mo behaviour during diagenesis. Porewater Mo tracks
691 diagenetic redox zones clearly in iron-rich pond sediments, and lower (0.5–1‰) sedimentary
692 δ^{98}Mo signatures are recorded at depth. Bioirrigation in these ponds can enrich the sediment
693 with Mo and extend the δ^{98}Mo signature acquired at the sediment-water interface to
694 sediments as deep as the limit of bioirrigation.
695
696 Differences in porewater Mo and its associated δ^{98}Mo reveal geochemical differences
697 between two pond sediments with similar dissolved sulfide profiles. In the intermediate pond
698 sediment, porewater enrichments of Mo and decoupled porewater and sediment δ^{98}Mo
699 suggest active redistribution of Mo as Fe and Mn oxides are broken down during diagenesis.
700 In sulfide-rich pond sediment, in the absence of reducible Fe and Mn oxides, the majority of
701 Mo has already been sequestered as $FeMoS_4$ so porewater Mo is controlled by solubility with
702 this phase. This argument is supported by both predictions from the model described in Helz
703 et al. (2011) and by similarities between sediment and porewater δ^{98}Mo occurring because of
704 solubility equilibrium.
705
706 Sedimentary δ^{98}Mo is higher in pond sediments containing aqueous sulfide than in pond
707 sediments containing ferrous iron. Given that iron-rich ponds transform to sulfide-rich ponds,
708 differences in δ^{98}Mo must reflect overprinting of the sediment Mo. This effect is expected to
709 be more rapid where residence time of Mo is shorter in the overlying water column. We
710 suggest that soft sediment diagenesis needs to be considered when interpreting δ^{98}Mo in past
711 and present systems.
712

Acknowledgements

Appendices and data

Appendix 1 – Salt marsh chemistry details

Appendix 2 – Model details

Appendix 3 – Supplementary figures

Research Data – Data table

References:

Algeo T. J. and Lyons T. W. (2006) Mo-total organic carbon covariation in modern anoxic marine environments: Implications for analysis of paleoredox and paleohydrographic conditions: MO-TOC COVARIATION IN ANOXIC SEDIMENTS. *Paleoceanography* **21**, n/a-n/a.

Antler G., Mills J. V., Hutchings A. M., Redeker K. R. and Turchyn A. V. (2019) The Sedimentary Carbon-Sulfur-Iron Interplay – A Lesson From East Anglian Salt Marsh Sediments. *Frontiers in Earth Science* **7**. Available at: https://www.frontiersin.org/article/10.3389/feart.2019.00140/full [Accessed September 4, 2019].

Arnold G. L. (2004) Molybdenum Isotope Evidence for Widespread Anoxia in Mid-Proterozoic Oceans. *Science* **304**, 87–90.

Barling J. and Anbar A. D. (2004) Molybdenum isotope fractionation during adsorption by manganese oxides. *Earth and Planetary Science Letters* **217**, 315–329.

Bethke C. M., Sanford R. A., Kirk M. F., Jin Q. and Flynn T. M. (2011) The thermodynamic ladder in geomicrobiology. *American Journal of Science* **311**, 183–210.

Canfield D. E., Raiswell R. and Bottrell S. H. (1992) The reactivity of sedimentary iron minerals toward sulfide. *American Journal of Science* **292**, 659–683.

Chappaz A., Lyons T. W., Gregory D. D., Reinhard C. T., Gill B. C., Li C. and Large R. R. (2014) Does pyrite act as an important host for molybdenum in modern and ancient euxinic sediments? *Geochimica et Cosmochimica Acta* **126**, 112–122.

Cline J. D. (1969) SPECTROPHOTOMETRIC DETERMINATION OF HYDROGEN SULFIDE IN NATURAL WATERS1. *Limnology and Oceanography* **14**, 454–458.

Dahl T. W., Anbar A. D., Gordon G. W., Rosing M. T., Frei R. and Canfield D. E. (2010) The behavior of molybdenum and its isotopes across the chemocline and in the sediments of sulfidic Lake Cadagno, Switzerland. *Geochimica et Cosmochimica Acta* **74**, 144–163.

Dahl T. W., Chappaz A., Hoek J., McKenzie C. J., Svane S. and Canfield D. E. (2017) Evidence of molybdenum association with particulate organic matter under sulfidic conditions. *Geobiology* **15**, 311–323.

Dickson A. J. (2017) A molybdenum-isotope perspective on Phanerozoic deoxygenation events. *Nature Geoscience* **10**, 721–726.

Dickson A. J., Jenkyns H. C., Porcelli D., van den Boorn S. and Idiz E. (2016) Basin-scale controls on the molybdenum-isotope composition of seawater during Oceanic Anoxic Event 2 (Late Cretaceous). *Geochimica et Cosmochimica Acta* **178**, 291–306.

Erickson B. E. and Helz G. R. (2000) Molybdenum(VI) speciation in sulfidic waters: Stability and lability of thiomolybdates. *Geochimica et Cosmochimica Acta* **64**, 1149–1158.

Goldberg T., Archer C., Vance D. and Poulton S. W. (2009) Mo isotope fractionation during adsorption to Fe (oxyhydr)oxides. *Geochimica et Cosmochimica Acta* **73**, 6502–6516.

Goldberg T., Archer C., Vance D., Thamdrup B., McAnena A. and Poulton S. W. (2012) Controls on Mo isotope fractionations in a Mn-rich anoxic marine sediment, Gullmar Fjord, Sweden. *Chemical Geology* **296–297**, 73–82.

Helz G. R., Bura-Nakić E., Mikac N. and Ciglenečki I. (2011) New model for molybdenum behavior in euxinic waters. *Chemical Geology* **284**, 323–332.

Helz G. R. and Vorlicek T. P. (2019) Precipitation of molybdenum from euxinic waters and the role of organic matter. *Chemical Geology* **509**, 178–193.

Hutchings A. M., Antler G., Wilkening J. V., Basu A., Bradbury H. J., Clegg J. A., Gorka M., Lin C. Y., Mills J. V., Pellerin A., Redeker K. R., Sun X. and Turchyn A. V. (2019) Creek Dynamics Determine Pond Subsurface Geochemical Heterogeneity in East Anglian (UK) Salt Marshes. *Frontiers in Earth Science* **7**. Available at: https://www.frontiersin.org/article/10.3389/feart.2019.00041/full [Accessed May 23, 2019].

Kendall B., Dahl T. W. and Anbar A. D. (2017) THE STABLE ISOTOPE GEOCHEMISTRY OF MOLYBDENUM. *Reviews in Mineralogy and Geochemistry* **82**, 683–732.

King E. K., Perakis S. S. and Pett-Ridge J. C. (2018) Molybdenum isotope fractionation during adsorption to organic matter. *Geochimica et Cosmochimica Acta* **222**, 584–598.

Lin C. Y., Turchyn A. V., Krylov A. and Antler G. (2019) The microbially driven formation of siderite in salt marsh sediments. *Geobiology*. Available at: https://onlinelibrary.wiley.com/doi/abs/10.1111/gbi.12371 [Accessed February 13, 2020].

Lyons T. W., Anbar A. D., Severmann S., Scott C. and Gill B. C. (2009) Tracking Euxinia in the Ancient Ocean: A Multiproxy Perspective and Proterozoic Case Study. *Annual Review of Earth and Planetary Sciences* **37**, 507–534.

McManus J., Berelson W. M., Severmann S., Poulson R. L., Hammond D. E., Klinkhammer G. P. and Holm C. (2006) Molybdenum and uranium geochemistry in continental margin sediments: Paleoproxy potential. *Geochimica et Cosmochimica Acta* **70**, 4643–4662.

McManus J., Nägler T. F., Siebert C., Wheat C. G. and Hammond D. E. (2002) Oceanic molybdenum isotope fractionation: Diagenesis and hydrothermal ridge-flank alteration: MOLYBDENUM ISOTOPE FRACTIONATION. *Geochemistry, Geophysics, Geosystems* **3**, 1–9.

Miller C. A., Peucker-Ehrenbrink B., Walker B. D. and Marcantonio F. (2011) Re-assessing the surface cycling of molybdenum and rhenium. *Geochimica et Cosmochimica Acta* **75**, 7146–7179.

Mills J. V., Antler G. and Turchyn A. V. (2016) Geochemical evidence for cryptic sulfur cycling in salt marsh sediments. *Earth and Planetary Science Letters* **453**, 23–32.

Nägler T. F., Anbar A. D., Archer C., Goldberg T., Gordon G. W., Greber N. D., Siebert C., Sohrin Y. and Vance D. (2013) Proposal for an International Molybdenum Isotope Measurement Standard and Data Representation. *Geostand Geoanal Res*, n/a-n/a.

Nägler T. F., Neubert N., Böttcher M. E., Dellwig O. and Schnetger B. (2011) Molybdenum isotope fractionation in pelagic euxinia: Evidence from the modern Black and Baltic Seas. *Chemical Geology* **289**, 1–11.

Nakagawa Y., Takano S., Firdaus M. L., Norisuye K., Hirata T., Vance D. and Sohrin Y. (2012) The molybdenum isotopic composition of the modern ocean. *GEOCHEMICAL JOURNAL* **46**, 131–141.

Neubert N., Nägler T. F. and Böttcher M. E. (2008) Sulfidity controls molybdenum isotope fractionation into euxinic sediments: Evidence from the modern Black Sea. *Geology* **36**, 775.

Pearce C. R., Cohen A. S. and Parkinson I. J. (2009) Quantitative Separation of Molybdenum and Rhenium from Geological Materials for Isotopic Determination by MC-ICP-MS. *Geostandards and Geoanalytical Research* **33**, 219–229.

Poulson Brucker R. L., McManus J., Severmann S. and Berelson W. M. (2009) Molybdenum behavior during early diagenesis: Insights from Mo isotopes: Mo ISOTOPES AND EARLY DIAGENESIS. *Geochemistry, Geophysics, Geosystems* **10**, n/a-n/a.

Poulson R. L., Siebert C., McManus J. and Berelson W. M. (2006) Authigenic molybdenum isotope signatures in marine sediments. *Geology* **34**, 617.

Pye K., Dickson J. A. D., Schiavon N., Coleman M. L. and Cox M. (1990) Formation of siderite-Mg-calcite-iron sulphide concretions in intertidal marsh and sandflat sediments, north Norfolk, England. *Sedimentology* **37**, 325–343.

Reinhard C. T., Planavsky N. J., Robbins L. J., Partin C. A., Gill B. C., Lalonde S. V., Bekker A., Konhauser K. O. and Lyons T. W. (2013) Proterozoic ocean redox and biogeochemical stasis. *Proceedings of the National Academy of Sciences* **110**, 5357–5362.

829   Scholz F., Baum M., Siebert C., Eroglu S., Dale A. W., Naumann M. and Sommer S. (2018)
830   Sedimentary molybdenum cycling in the aftermath of seawater inflow to the
831   intermittently euxinic Gotland Deep, Central Baltic Sea. *Chemical Geology* **491**, 27–
832   38.

833   Scholz F., McManus J. and Sommer S. (2013) The manganese and iron shuttle in a modern
834   euxinic basin and implications for molybdenum cycling at euxinic ocean margins.
835   *Chemical Geology* **355**, 56–68.

836   Scholz F., Siebert C., Dale A. W. and Frank M. (2017) Intense molybdenum accumulation in
837   sediments underneath a nitrogenous water column and implications for the
838   reconstruction of paleo-redox conditions based on molybdenum isotopes. *Geochimica*
839   *et Cosmochimica Acta* **213**, 400–417.

840   Scott C. and Lyons T. W. (2012) Contrasting molybdenum cycling and isotopic properties in
841   euxinic versus non-euxinic sediments and sedimentary rocks: Refining the
842   paleoproxies. *Chemical Geology* **324–325**, 19–27.

843   Shaw T. J., Gieskes J. M. and Jahnke R. A. (1990) Early diagenesis in differing depositional
844   environments: The response of transition metals in pore water. *Geochimica et*
845   *Cosmochimica Acta* **54**, 1233–1246.

846   Siebert C., Nägler T. F., von Blanckenburg F. and Kramers J. D. (2003) Molybdenum isotope
847   records as a potential new proxy for paleoceanography. *Earth and Planetary Science*
848   *Letters* **211**, 159–171.

849   Skierszkan E. K., Robertson J. M., Lindsay M. B. J., Stockwell J. S., Dockrey J. W., Das S.,
850   Weis D., Beckie R. D. and Mayer K. U. (2019) Tracing Molybdenum Attenuation in
851   Mining Environments Using Molybdenum Stable Isotopes. *Environmental Science &*
852   *Technology* **53**, 5678–5686.

853   Skierszkan E. K., Stockwell J. S., Dockrey J. W., Weis D., Beckie R. D. and Mayer K. U.
854   (2017) Molybdenum (Mo) stable isotopic variations as indicators of Mo attenuation in
855   mine waste-rock drainage. *Applied Geochemistry* **87**, 71–83.

856   Stookey L. L. (1970) Ferrozine---a new spectrophotometric reagent for iron. *Analytical*
857   *Chemistry* **42**, 779–781.

858   van de Velde S. J., Hidalgo-Martinez S., Callebaut I., Antler G., James R. K., Leermakers M.
859   and Meysman F. J. R. (2020) Burrowing fauna mediate alternative stable states in the
860   redox cycling of salt marsh sediments. *Geochimica et Cosmochimica Acta* **276**, 31–
861   49.

862   Vorlicek T. P., Helz G. R., Chappaz A., Vue P., Vezina A. and Hunter W. (2018)
863   Molybdenum Burial Mechanism in Sulfidic Sediments: Iron-Sulfide Pathway. *ACS*
864   *Earth and Space Chemistry* **2**, 565–576.

865   Wasylenki L. E., Weeks C. L., Bargar J. R., Spiro T. G., Hein J. R. and Anbar A. D. (2011)
866   The molecular mechanism of Mo isotope fractionation during adsorption to birnessite.
867   *Geochimica et Cosmochimica Acta* **75**, 5019–5031.

868 Wilkening J. V., Turchyn A. V., Redeker K. R., Mills J. V., Antler G., Carrión O. and Todd
869   J. D. (2019) The Production and Fate of Volatile Organosulfur Compounds in Sulfidic
870   and Ferruginous Sediment. *Journal of Geophysical Research: Biogeosciences* **124**,
871   3390–3402.

872 Xu N., Christodoulatos C. and Braida W. (2006) Adsorption of molybdate and
873   tetrathiomolybdate onto pyrite and goethite: Effect of pH and competitive anions.
874   *Chemosphere* **62**, 1726–1735.

875

876

877